Biosensors and Bioelectronics 144 (2019) 111697

Contents lists available at ScienceDirect

Biosensors and Bioelectronics

journal homepage: www.elsevier.com/locate/bios

A 2D transition metal carbide MXene-based SPR biosensor for ultrasensitive carcinoembryonic antigen detection

Qiong Wu[a,b], Ningbo Li[a], Ying Wang[a], Ying liu[a], Yanchao Xu[a], Shuting Wei[a], Jiandong Wu[a], Guangri Jia[a], Xuedong Fang[b], Fangfang Chen[b,**], Xiaoqiang Cui[a,*]

[a] School of Materials Science and Engineering, State Key Laboratory of Automotive Simulation and Control and Key Laboratory of Automobile Materials of MOE, Jilin University, 2699 Qianjin Street, Changchun, 130012, Jilin, China

[b] Department of Gastrointestinal and Colorectal Surgery, China-Japan Union Hospital of Jilin University, 126 Sendai Street, Changchun, 130033, Jilin, China

ARTICLE INFO

Keywords:
Surface plasmon resonance (SPR)
Carcinoembryonic antigen (CEA)
Immunoassay
2D materials
MXene

ABSTRACT

Surface plasmon resonance (SPR) has become a leading technique for in situ bioaffinity assay of diverse targets without need of fluorescent or enzymatic labeling. Nanomaterials-enhanced SPR sensors have developed rapidly and widened the application scope of SPR sensing technology. In this report we describe an ultrasensitive SPR biosensor for detecting carcinoembryonic antigen (CEA). Our SPR biosensor utilizes a Ti_3C_2-MXene-based sensing platform and multi-walled carbon nanotube (MWCNTs)-polydopamine (PDA)-Ag nanoparticle (AgNPs) signal enhancer. Ti_3C_2-MXene, a new class of two-dimensional (2D) transition metal carbides, offers a large hydrophilic-biocompatible surface ideal for SPR biosensing. Ti_3C_2-MXene/AuNPs composites after synthesis are then decorated with staphylococcal protein A (SPA) to orient and immobilize monoclonal anti-CEA antibody (Ab_1) through its Fc region. By introducing MWCNTs-PDA-AgNPs-polyclonal anti-CEA antibody (MWPAg-Ab_2) conjugate combined with a sandwich format, the present method provides a dynamic range for CEA determination of 2×10^{-16} to 2×10^{-8} M and a detection limit of 0.07 fM. This biosensing approach demonstrates good reproducibility and high specificity for CEA in real serum samples providing a promising method to evaluate CEA in human serum for early diagnosis and monitoring of cancer.

1. Introduction

Malignant cancers have become one of the greatest threats to human health. Early diagnosis of cancer is important since it offers opportunities to extend patient lives. Tumor markers exist in tumor cells themselves or are secreted by tumor cells. In either case the presence of these tumor markers above baseline may suggest the existence and growth of tumor (Wei et al., 2019). Carcinoembryonic antigen (CEA) is a widely used tumor marker, which elevates in many malignancies, such as gastric cancer, colorectal cancer, breast cancer, liver cancer and pancreatic cancer. Serum CEA is used in clinical research to identify early disease, monitor tumor recurrence and metastatic disease (Ren et al., 2017). The normal range of serum CEA in healthy adults is below 5.0 ng mL^{-1}, but increases rapidly when normal cells become cancerous (Lv et al., 2018b).

Many methods have been reported for the detection of CEA including colorimetric immunoassay (Jia et al., 2019), fluorescent immunoassay (Wang et al., 2019), surface-enhanced Raman scattering (Bai et al., 2019), electrochemiluminescence immunoassay (Jie et al., 2018) and electrochemical immunoassay (Kumar et al., 2019). These methods usually have drawbacks such as high cost, poor stability, complicated protocols and poor specificity. In contrast to these other methods, surface plasmon resonance technology offers label-free and real-time detection, high sensitivity and selectivity, ease of miniaturization and rapid detection making it well suited for bioassays. Nanomaterial-enhanced SPR sensing strategy greatly facilitates the improvement of sensing properties and employed as effective tools to sense hard-to-detect molecules within the concentration range between pmol and amol (Zeng et al., 2014). Fabricating SPR biosensors for ultrasensitive and selective detection of CEA can be expected to be promising.

Two dimensional (2D) layered materials own large surface area and anisotropic electron transport behavior, making them potential transducer materials for applications in biosensing (Taniselass et al., 2019; Morales-Narváez et al., 2019; Majd et al., 2018; Cai et al., 2018; Chand et al., 2018). 2D materials families have expanded quickly introducing

* Corresponding author.
** Corresponding author.
E-mail address: xqcui@jlu.edu.cn (X. Cui).

https://doi.org/10.1016/j.bios.2019.111697
Received 19 July 2019; Received in revised form 7 September 2019; Accepted 9 September 2019
Available online 10 September 2019
0956-5663/

graphene (Parate et al., 2019; Khalil et al., 2019), MoS_2 (Li et al., 2019; Wu et al., 2018a), and black phosphorous (BP) (Yuan et al., 2018b; Chen et al., 2017). MXenes, an emerging 2D nanomaterial with graphene-like structure, have shown great promise in the field of catalysis (Djire et al., 2019), clean energy (Jun et al., 2019), electronics (VahidMohammadi et al., 2019), fuel cells (Xiao et al., 2019), and supercapacitors (Xu et al., 2019). MXenes including early transition metal carbides, nitrides and carbonitrides can be produced by exfoliation of selective MAX phases. MAX phase corresponds to the general formula $M_{n+1}AX_n$ (n = 1, 2, 3) where M represents early d-block transition metals, A layer refers to the element from the group IIIA or IVA in the periodic table, and X is either C or N atoms (Peng et al., 2019). Ti_3C_2-MXene is the first-prepared MXene with reports of its performance in batteries (Tian et al., 2019), supercapacitors (Oyedotun et al., 2019), electro-and photo catalysis (Tie et al., 2019), biology (Zhang et al., 2018) and sensors (Muckley et al., 2018). Monolayer or few-layer Ti_3C_2-MXene nanosheets have been constructed utilizing a two-step exfoliation process that includes hydrofluoric acid (HF) etching followed by organic base intercalation (Xuan et al., 2016; Lin et al., 2017). The surface of Ti_3C_2-MXene is easily terminated with various functional groups (e.g., –O, –OH or/and –F group) during the etching procedure without changing its metallic conductivity (He et al., 2019). It is more advantageous to keep Ti_3C_2-MXene stable due to the strong bonds between the Ti and the surface-functionalized groups. Ti_3C_2-MXene displays advantages of excellent electrical conductivity, hydrophilicity, complete metal atomic layers, ultrathin 2D sheet-like morphology, large surface area, ease of functionalization, high stability, excellent mechanical properties and good bio-compatibility. These good properties of Ti_3C_2-MXene distinguish it from traditional 2D materials and suggest biosensing applications. To date, biosensors based on MXenes have been developed and employed to detect nitrite (Liu et al., 2015), pesticides (Zhou et al., 2017), phenol (Wu et al., 2018b) and H_2O_2 (Lorencova et al., 2018). However, there are only a few reports using MXene in SPR biosensing technology.

Here, we propose using Ti_3C_2-MXene/AuNPs/SPA as biosensing platform to improve detection sensitivity. Ultrathin Ti_3C_2-MXene nanosheets are the substrate for binding AuNPs. The AuNPs now on the surface of Ti_3C_2-MXene/AuNPs composites are further modified with SPA to orient and immobilize monoclonal anti-CEA antibodies (Ab_1) used to capture the analyte CEA. Multi-walled carbon nanotube (MWCNTs)-polydopamine (PDA)-AgNPs (MWPAg) nanohybrids conjugated with polyclonal anti-CEA antibodies (Ab_2) termed MWPAg-Ab_2. MWPAg-Ab_2 is then introduced into the sensing system and functions as a signal enhancer to further improve the sensitivity. The resulting Ti_3C_2-MXene based biosensor shows ultrasensitive response to CEA biomarker with good selectivity, good reproducibility and high recoveries in human serum samples.

2. Materials and methods

2.1. Materials

Monoclonal and polyclonal carcinoembryonic antibodies (anti-CEA) and carcinoembryonic antigen (CEA) were purchased from Fitzgerald Industries. Bovine serum albumin (BSA) was purchased from Ding Guo Biotechnology Company. Ti_3AlC_2 MAX phase was purchased from Carbon-Ukraine ltd. Hydrogen tetrachloroauratehydrate ($HAuCl_4 \cdot 3H_2O$) was purchased from Acros. Sodium borohydride ($NaBH_4$), hydrofluoric acid and ethanol were purchased from Sinopharm Chemical Reagent Co., Ltd. Human serum samples were supplied by China-Japan Union Hospital of Jilin University. Sodium phosphate buffered saline (PBS, 0.01 mol L^{-1}, pH 7.4) and tris-buffer (10 mmol L^{-1}, pH 8.5) were prepared before use. All other chemicals were of analytical grade and used without purification. All water was prepared using a Millipore purification device. Anti-CEA and CEA were stored at -20 °C. All other biological reagents were stored at 4 °C.

2.2. Equipment

All SPR measurements in this work were performed using an angle modulation SPR biosensor. The set-up was based on the conventional Kretchmann configuration and it consists of a He–Ne laser of wavelength λ = 632.8 nm, a light guide system, a prism-sensing unit, a flow cell reactor, a miniature spectrometer, and a data-processing system. The light emitting from He–Ne laser was paralleled and polarized by a collimator combined with a polarizer. The light was then guided to an optical prism (LAFSN9 glass, ε = 3.40) equipped with a SPR chip to excite surface plasmon at the interface of metal and sample solution. The resonant angle was determined by using a TR2005 spectrometer (RES-TEC resonant sensor technology, Germany). The assay was based on an increasing refractive index caused by the capture of analytes on the sensing membrane which led to a redshift of resonant angle in the SPR spectrum.

2.3. Characterization

Sample components were analyzed by the X-ray diffraction (XRD) using a Bragg-Brentano diffractometer (D8-tools, Germany) with a Cu Kα (λ = 0.15418 nm) emitting source. X-ray photoelectron spectroscopy (XPS) was conducted on an Escalab-250 instrument (Thermo Fisher Scientific, USA) with a hemisphere detector and a monochromatic Al Kα radiation source (1486.6 eV). UV-Vis absorption spectra of the samples were recorded on a TU-1810C UV-Vis spectrometer (Beijing Purkinje General Instrument Co., Ltd.). The samples morphologies were characterized employing a scanning electron microscope (SEM JEOL JSM6700F, Japan), a transmission electron microscope (TEM JEOL JEM-2000EX, Japan), and an atomic force microscope (AFM) with ScanAsyst in air mode (Bruker Co., Germany).

2.4. Synthesis of Ti_3C_2-MXene-AuNPs nanocomposites

Ti_3C_2-MXene was synthesized by etching bulk Ti_3AlC_2 as previously described with minor modifications (Alhabeb et al., 2017). Typically, 1.0 g of Ti_3AlC_2 powder was added to 20 mL of 30% hydrochloric acid (HF) and stirred for 12 h at room temperature. The product was washed with deionized water (DI water) three times and collected by centrifuging at 8000 rpm. The precipitate was dried at 65 °C for 12 h. Ti_3C_2-MXene (200 mg) was dispersed in 10 mL of TMAOH (25%) and stirred for 5 h at 500 r min^{-1}. The dark green supernatant was centrifuged at 16000 rpm for 30 min to collect the precipitate. The final product was then dispersed in 25 mL of DI water. Ti_3C_2-MXene nanosheets were decorated with AuNPs using a chemical reduction method. 60 μL of $HAuCl_4 \cdot 3H_2O$ solution (0.1 g mL^{-1}) was added to 12 mL of Ti_3C_2-MXene (0.5 mg mL^{-1}) solution and then a mixture of 0.16 M $NaBH_4$ and 1.6 M NaOH (50 μL) used as reducing agent was added to the above solution with rapid stirring. The mixture was stirred at 1000 r min^{-1} for 30 min. The solution was washed three times with DI water. The final precipitate was redispersed in 10 mL of DI water. In the application process, 100 μL of SPA (1 mg mL^{-1}) was added into 3 mL of Ti_3C_2-MXene/AuNPs solution and kept for 3 h at 4 °C. Excess SPA in the solution were removed by centrifugation at 10000 rpm for 10 min and dispersed in 3 mL of DI water. AuNPs were synthesized according to the Frens' method (Frens, 1973). AuNPs modified with SPA were prepared by the same procedure of Ti_3C_2-MXene/AuNPs.

2.5. Synthesis of MWCNTs-PDA-AgNPs-Ab_2 nanocomposite

The MWPAg nanohybrids were prepared according to a one-pot procedure (Lin et al., 2014). MWPAg-Ab_2 nanoconjugates were obtained by adding 500 μg of Ab_2 into 10 mL of MWPAg solution under soft stirring at room temperature for 24 h. The Ab_2 can be attached strongly to the surface of MWPAg by Schiff-base reaction between amino residues of Ab_2 and quinones groups formed in PDA. The

resultant solution was redispersed in PBS containing 10 mg mL^{-1} BSA to block the nonbinding sites. MWCNTs-PDA nanocomposites were prepared by the same method without addition of $AgNO_3$ solution.

2.6. Fabrication of Ti_3C_2-MXene/AuNPs-based sensing platform

The glass slide coated with gold film was fixed in the bottom of the reactor to form a flow chamber. Firstly, 500 μL of the prepared Ti_3C_2-MXene/AuNPs/SPA composite solution was injected into the flow cell filled with DI water and incubated for 3 h at room temperature completing the assembly of Ti_3C_2-MXene/AuNPs/SPA composites on bare Au film. Subsequently, DI water was injected to wash away unbounded Ti_3C_2-MXene/AuNPs/SPA composites, and then PBS was injected into the flow cell and used as the baseline solution. After the resonant angle stabilized, 500 μL of Ab_1 diluted with PBS (100 μg mL^{-1}) was injected into the flow cell to achieve oriented integration with SPA on the surfaces of the Ti_3C_2-MXene/AuNPs nanohybrids. Next, unbound Ab_1 was removed by washing with PBS. This was followed using 10 mg mL^{-1} BSA solution in PBS to block non-specific binding sites on the sensing membrane. After 20 min, PBS was injected into the flow cell to wash off the unbound BSA and the obtained sensing platform was used to capture CEA in samples.

2.7. SPR assay

Different concentrations of CEA diluted with PBS (500 μL) was separately injected into the flow cell over the sensing film with immobilized Ab_1 and incubated for 30 min. PBS was then injected into the flow cell to remove the unbound CEA. After the resonant angle was stable (about 5 min), 500 μL of 0.4 mg mL^{-1} MWPAg-Ab_2 composites was injected into the flow cell and kept for 20 min. The sensor responses were determined as the shifts of resonant angle before sample injection and after rinsing with PBS. The whole assay was conducted under normal temperature and pressure, and all experiments were repeated three times. A schematic of our proposed biosensor is displayed in Fig. 1.

3. Results and discussion

3.1. Characterization

The Ti_3C_2-MXene/AuNPs nanocomposites employed as sensing platform in this work were characterized by XRD, XPS, SEM, AFM and UV-Vis absorption spectrum. In the XRD analysis, the Ti_3C_2-MXene and Ti_3C_2-MXene/AuNPs nanocomposites were scanned over the 2θ range of 5–80° (Fig. 2a). For Ti_3C_2-MXene, there were several very sharp diffraction peaks located at 6.1°, 18.16°, 25.64°, 30.36°, 36.02°, 36.62°, 41.84°, 43.0° and 60.62° in good agreement with the previously reported XRD spectra of $Ti_3C_2(OH)_2$ (Wu et al., 2018a). For Ti_3C_2-MXene/AuNPs nanocomposite, all the new emerging diffraction peaks in the XRD pattern corresponded to the (111), (200), (220) and (311) planes of the AuNPs, revealing successful hybridization.

XPS analysis was also used to confirm the composition of Ti_3C_2-MXene/AuNPs nanocomposites. The high resolution Ti 2p spectrum (Fig. 2c) resolved into two sets of double peaks, attributable to the Ti–O (464.0 and 458.2 eV) and Ti–C (464.8 and 458.75 eV) species, respectively. Our XPS results agree with those reported previously for Ti_3C_2-MXene (Naguib et al., 2011). Au 4f spectrum (Fig. 2d) resolved into two spin-orbit components. The two peaks had binding energies of 83.8 eV and 87.5 eV corresponding to the Au $4f_{7/2}$ and $4f_{5/2}$ peaks of metallic gold, (Hedman et al., 1971; Turner et al., 1990). These results provide further evidence of the formation of Ti_3C_2-MXene/AuNPs nanohybrids.

Ti_3C_2-MXene nanosheets were synthesized by exfoliating Al layer from the pristine Ti_3AlC_2 phases with HF at room temperature. Parent MAX-phase ceramics (Fig. S1a) underwent multilayer-stacked MXenes transition states (Fig. S1b) and then achieved few-layer or single-layer MXenes. Through the procedures of delamination by hydrofluoric acid (HF) etching and disintegration by organic base molecules intercalation and probe sonication breakage, the synthesized Ti_3C_2-MXene nanosheet is gauzy and wrinkled (Fig. S1c). The AFM image (Fig. 2b) suggests that the thickness of Ti_3C_2-MXene nanosheets is about 2 nm, consistent with a single-layer Ti_3C_2-MXene nanosheet as previously reported (Zhang et al., 2019).

The surfaces of the as-prepared Ti_3C_2-MXene nanosheets were decorated with AuNPs by the reduction of $HAuCl_4$. Dense AuNPs with average particle size of 40 nm were distributed uniformly on the surface of exfoliated, extremely thin and transparent MXene nanosheets (Fig. 3a). No isolated/free-standing gold nanostructures existed from the SEM image of Ti_3C_2-MXene/AuNPs composite (Fig. 3b). Energy dispersive X-ray spectroscopy (EDS) measurement was performed on the same area analyzed by SEM. The corresponding element-mapping images showed that the Ti, C, and Au elements were uniformly distributed, indicating the presence of the AuNPs on the surface of Ti_3C_2-MXene (Fig. S2). The Au content in Ti_3C_2-MXene/AuNPs composite was determined to be 54.6% by ICP measurement. For demonstrating the role of Ti_3C_2-MXene for sensitivity enhancement, bare AuNPs with similar diameter were synthesized. The prepared AuNPs were almost homogeneous and presents cluster-like morphology with rougher surface after attaching SPA (Fig. S3). The UV-Vis absorption peak position of bare AuNPs is 530 nm and the peak position of AuNPs in Ti_3C_2-MXene/AuNPs nanohybrids located at 565 nm due to the surface electron loss in Au during the formation of complexes. With the attachment of SPA, the adsorption peak position of bare AuNPs and AuNPs in Ti_3C_2-MXene/AuNPs redshifted 4 nm and 7 nm, respectively (Fig. S4). This suggests the formation of Ti_3C_2-MXene/AuNPs/SPA and AuNPs/SPA nanocomplexs.

MWPAg can be obtained by a one-pot synthesis, in which DA self-polymerized on the surface of MWCNTs to form PDA thin film, and Ag^+ was reduced in situ to AgNPs through the reduction of PDA. MWCNTs-PDA nanohybrids without AgNPs were synthesized to compare with the sensing performance obtained by MWPAg nanohybrids. Obviously, MWCNTs with multi-walled, thin long tubular mesh structure were coated with a thin film (Fig. S5). Dense AgNPs (average diameter, 30 nm) distributed well on the surfaces of MWCNTs-PDA nanohybrids after addition of Ag^+, and no free microspheres existed in the image (Fig. 3c). UV-Vis absorption spectrum of MWPAg composites showed the characteristic adsorption peak of AgNPs at 405 nm. A typical absorption peak of protein located at 280 nm appeared after MWPAg composites were conjugated with Ab_2 (Fig. S6). In addition, redshift of the peak position of AgNPs from 405 nm to 419 nm suggests the attachment of segmental Ab_2 to the surfaces of AgNPs through the interaction between Ag and amine groups of Ab_2.

3.2. Immobilization of mouse anti-CEA

Staphylococcal protein A (SPA), a polypeptide of staphylococcus, is able to bind selectively with the Fc regions of antibodies enabling a more favorable orientation of antibodies than adsorption, covalent binding, or cross-linking (Wu et al., 2015). Moreover, antigen-binding sites located on the distal ends of the Fab variable regions are retained for further capture of antigen (Vashist et al., 2011). Besides the highly ordered immobilization of Ab_1 on the sensor surface, Ti_3C_2-MXene/AuNPs decorated by SPA can be directly attached on the bare Au film without further processing due to the high association constant of Au-SPA complexes (Tang et al., 2006). The SPR spectra of Ti_3C_2-MXene/AuNPs/SPA sensing platform before and after 10 times washing were provided in Fig. S7. The negligible change of resonant angle further demonstrates the stability of the prepared sensing platform on bare Au film. After Ti_3C_2-MXene/AuNPs/SPA nanocomposites were assembled on Au film, 100 μg mL^{-1} Ab_1 were injected into the reactor. The SPR angle position is closely correlated with changes of the refractive index on the sensing chip surface. SPR signal increased with the capture of

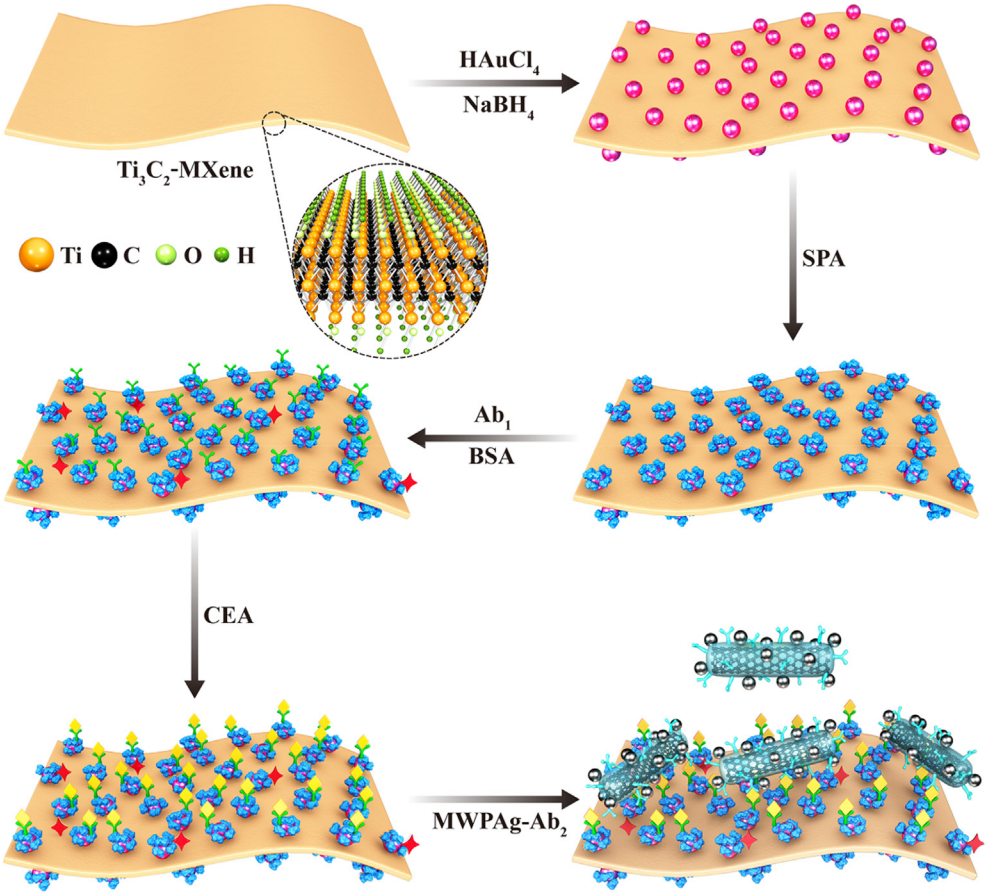

Fig. 1. Schematic showing the detection procedure of the proposed biosensor.

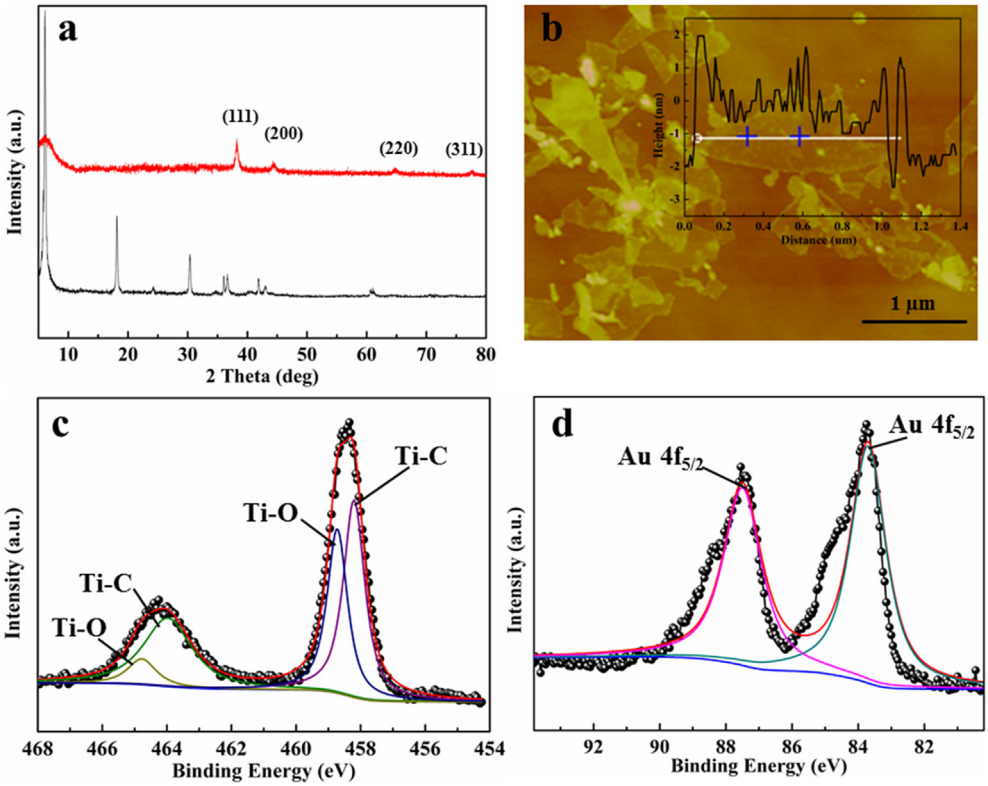

Fig. 2. XRD images of Ti_3C_2-MXene and Ti_3C_2-MXene/AuNPs (a), AFM image of Ti_3C_2-MXene (b) and High-resolution XPS spectra of Ti (c) and Au (d) of Ti_3C_2-MXene/AuNPs composite nanosheets.

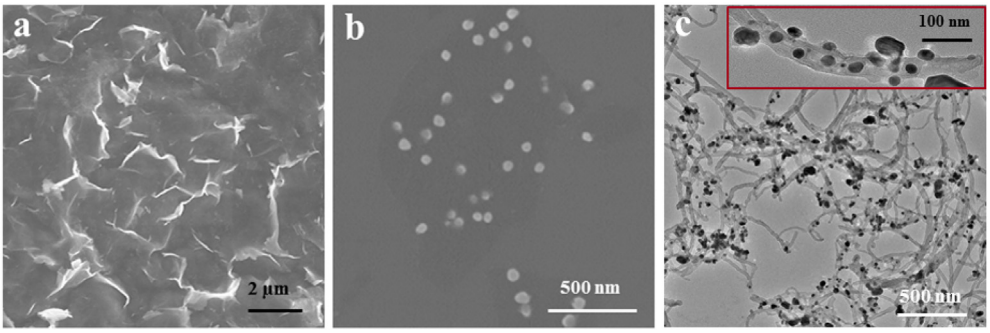

Fig. 3. SEM image of Ti_3C_2-MXene nanosheets (a), SEM image of Ti_3C_2-MXene/AuNPs nanosheets (b) and TEM image of MWPAg nanocomposites (c). Inset shows HRTEM image of MWPAg nanocomposites.

Ab_1 in solution and reached a plateau after 60 min, indicating that the immobilization of antibodies on the surface of Ti_3C_2-MXene/AuNPs/SPA was completed within 60 min. The dosage of antibodies was further optimized by monitoring the changes of SPR angles (Δθ) resulting from flowing a series of concentrations of Ab_1 over the sensing chip surface. The resonant angles were red-shifted with the increase of the concentration of Ab_1 (Fig. S8). The maximum SPR angle shifts for immobilizing Ab_1 was achieved at concentration of 100 μg mL^{-1}. Increasing the concentration to 125 μg mL^{-1}, the resonant angle showed no obvious shift, indicating that Ab_1 immobilized on Ti_3C_2-MXene/AuNPs/SPA sheets had reached saturation. Therefore, 100 μg mL^{-1} is selected to be the concentration of Ab_1 in the following experiments.

3.3. Steps to improve sensitivity of the technology

It is advantageous to conjugate more antibodies when Ti_3C_2-MXene is used as carrier. The surface of Ti_3C_2-MXene nanosheet is rough and abundant of oxygen-containing groups, so it owns large surface area and high loading capacity. The dense AuNPs modified by SPA deposited well on the Ti_3C_2-MXene nanosheets, which provide a novel platform for possessing abundant binding sites and oriented immobilization of antibodies. To further improve the sensitivity for detecting CEA, the classical sandwich strategy was employed in this work. MWPAg nanocomposites decorated with Ab_2 as signal enhancers were introduced into the sensing system to interact with CEA captured on the surface of the sensing chip. The MWPAg-Ab_2 nanoconjugates markedly enlarge the mass transferred on the surface of sensing chip and increase the refractive index of the sensing chip thereby amplifying the response signal. Moreover, the electromagnetic coupling between the high mass-density AgNPs and the underlying Au film leads to the amplification of the SPR signals originating from the dielectric changes of the substrate upon binding of the antigen-antibody complexes. As the amount of MWPAg-Ab_2 nanoconjugates is linked to sensitivity enhancement, we optimized the amount of MWPAg-Ab_2 nanoconjugates to be used in final assay. Using our standard assay protocol, resonant angle shifts for detecting 2×10^{-8} M CEA were measured with different concentration of MWPAg-Ab_2 nanoconjugates. The resonant angle displayed increasing redshifts with the injection of increasing amounts of MWPAg-Ab_2 nanoconjugates up to a final concentration of 0.4 mg mL^{-1}, suggesting that saturation had been reached (Fig. S9). This result indicates that a final concentration of MWPAg-Ab_2 nanoconjugates (0.4 mg mL^{-1}) was selected as the optimum concentration of MWPAg-Ab_2 signal enhancer in all experiments reported below. The maximum resonant angle shift increased to 369 mdeg resulting in a 146% increase over that of sensing system without MWPAg-Ab_2.

In addition, control experiments based on traditional 3-mercaptopropionic acid (MPA) modified sensing platform, AuNPs/SPA composites modified sensing platform, Ti_3C_2-MXene/AuNPs/SPA modified sensing platform, Ti_3C_2-MXene/AuNPs/SPA modified sensing platform combined with MWCNTs-PDA-Ab_2 signal enhancer, and Ti_3C_2-MXene/AuNPs/SPA modified sensing platform combined with MWPAg-Ab_2 signal enhancer were performed to determine 2×10^{-8} M CEA analyte for investigating the role of each component in sensitivity enhancement. It is clearly that SPR response signal increased with the perfection of sensing structure (Fig. S10). For the sensing platform, Ti_3C_2-MXene nanosheets offer large surface area for loading dense AuNPs-SPA without aggregation, and SPA molecules enable oriented immobilization of antibodies, which benefit well for immobilizing more antibodies and protecting their binding sites, enhancing the sensitivity. Then, MWPAg-Ab_2 conjugates signal enhancers were introduced to the sensing system to further amplify the response signals. MWCNTs-PDA-Ab_2 nanoconjugates captured on the surface of sensing chip effectively increase the refractive index of the sensing chip. Besides, the PDA-induced spontaneous Ag reductive deposition on the surface of MWCNTs further increases the mass on the sensing chip, and the electromagnetic coupling between AgNPs and the underlying Au film could also amplify the response signals. The synergistic effect of the whole sensing structure leads to the prominent sensitivity enhancement.

3.4. Sensitivity of the assay

Since the SPR response signal linearly increased with the logarithm

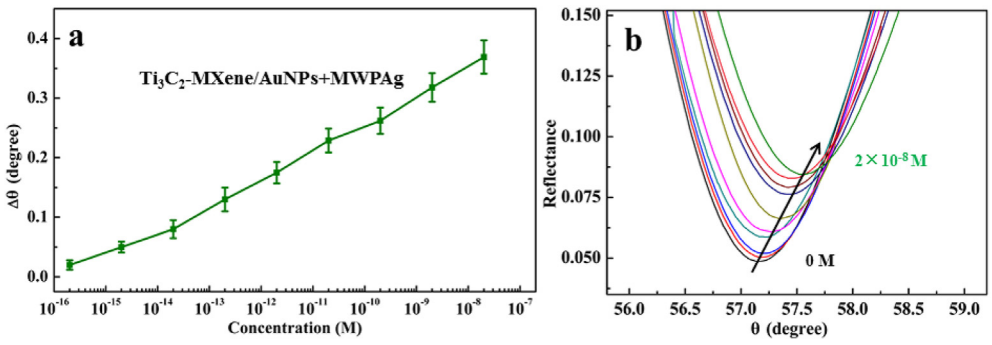

Fig. 4. Relationship between SPR signal changes and CEA concentrations obtained by biosensor based on Ti_3C_2-MXene/AuNPs sensing platform and MWPAg-Ab_2 signal enhancer. Each point corresponds to the SPR response shift for the concentration of CEA analyte (a) and SPR spectra of CEA with different concentrations (2×10^{-16} to 2×10^{-8} M) with the proposed biosensor (b).

Table 1
Comparison of analytical performance obtained by current work and those reported in the literature.

Method	Detection range (pM)	Detection limit (fM)	References
ECL	0.0005–400	0.225	Yuan et al. (2018a)
Electrochemical	5–25000	1050	Paniagua et al. (2019)
Fluorescence	0.15–30	39.5	Wang et al. (2019)
PEC	0.05–250	16	Han et al. (2018)
Electrochemical	0.0025–250	0.835	Lv et al. (2018a)
PEC	0.0025–250	0.7	Nie et al. (2018)
Electrochemical	0.125–125	2.5	Tran et al. (2018)
Photoelectrochemical	0.005–200	2.5	Hu et al. (2018)
SPR	5–1250	1500	Guo et al. (2017)
SPR	0.5–5000	500	Wang et al. (2016)
SPR	0.0002–20000	0.07	This work

of CEA concentration in the range from 2×10^{-16} M to 2×10^{-8} M (Fig. 4a), the relative resonant angle change ($\Delta\theta$) could be expressed as a function of CEA concentration. The linear relationship can be described as $\Delta\theta = 0.7007 + 0.0193$ lnC, (lnC is the natural logarithm of the CEA concentration) with a correlation coefficient of $R^2 = 0.9989$ (Fig. S11). The detection limit is 0.07 fM at a signal-to-noise ratio of 3 s (where s is the standard deviation of the blank solution, n = 10), which is lower than those reported CEA detection assays (Table 1). The corresponding SPR spectra of detection of CEA with concentrations ranging from 2×10^{-16} M to 2×10^{-8} M via the proposed biosensor were provided in Fig. 4b.

Moreover, the reproducibility of the proposed method were studied with the relative standard deviation (RSD), which were evaluated by independent testing of each sample in triplicate, and the obtained RSDs of this biosensor for CEA were less than 5% (Fig. 4a), demonstrating its well reproducibility. The stability of the fabricated sensing platform was also investigated by measuring the SPR responses to 10^{-12} M CEA concentration over the period of 7 days, during which the sensing platform was stored at 4 °C. As shown in Fig. S12, our biosensor lost 13% of its initial activity after storing for 7 days.

3.5. Recoveries of method in serum

Selectivity and sensitivity are important performance parameters of biosensors especially for analyzing complex samples. Control experiments were conducted by analyzing blank samples without CEA to evaluate the nonspecific adsorption of MWCNTs-PDA-Ab_2 and MWPAg-Ab_2, respectively. The near zero resonant angle shift confirms negligible nonspecific interaction between signal enhancers and the sensing chip surface (Fig. S13). To explore interference from nonspecific adsorption of matrix proteins in the determination of real samples, the present sensing strategy was applied to analyze CEA spiked-healthy human serum samples diluted with PBS for 10 times (Table 2). Recoveries ranged from 98.2% to 111.1% with RSDs of 4.9–8.2%, suggesting that the accuracy and reproducibility of the present method are acceptable.

3.6. Clinical diagnosis

To validate feasibility of the proposed biosensor for practical clinical applications, five cancer patients' serum samples (two cases of rectal cancer and three cases of colon cancer obtained from China-Japan Union Hospital of Jilin University) were analyzed for CEA using a commercial ELISA method for comparison. The obtained relative deviations between our method and ELISA method were from 2.7 to 14.0% (Table S1), revealing that the proposed biosensor presents great promise as a reliable tool for application in clinical diagnosis of cancer.

Table 2
Analytical results of CEA in human serum (n = 3).

Content of CEA (ng mL^{-1})	Spiked (ng mL^{-1})	Shifts in serum (nm)	Recovery (%)	RSD (%)
None	10000	9640	96.4	6.7
None	1000	1035	103.5	5.4
None	10	9.4	94	8.2
None	0.1	0.09	90	4.9

4. Conclusion

In summary, 2D Ti_3C_2-MXene nanosheets were prepared by exfoliating pristine Ti_3AlC_2 with HF and used as a biosensing material to fabricate an SPR biosensor for detecting the broad spectrum tumor marker, CEA. The prepared Ti_3C_2-MXene/AuNPs/SPA-based sensing platform is easy to prepare, convenient to operate, and provides high sensitivity and selectivity. MWPAg nanohybrids conjugated with polyclonal antibodies as response signal enhancers improves detection sensitivity, and the proposed SPR biosensor shows an ultralow detection limit of 0.07 fM. The sensing strategy presented here for detecting CEA can be easily expanded to the measurement of other analytes which have available corresponding epitopes. The high recoveries of spiked human serum samples suggest good selectivity in complex mixtures. Our work on the preparation and application of Ti_3C_2-MXene-based SPR sensing platform for cancer biomarker detection has important significance for broadening the application fields of MXenes and demonstrates its potential use in biomedical applications. We note that there are limitations for the present biosensor commercial application including the time-consuming fabrication prior to analysis, which is also a key technology focus in our future research.

CRediT authorship contribution statement

Qiong Wu: Investigation, Writing - original draft, Data curation. **Ningbo Li:** Methodology, Supervision. **Ying Wang:** Methodology, Supervision. **Ying liu:** Methodology, Supervision. **Yanchao Xu:** Data curation. **Shuting Wei:** Data curation. **Jiandong Wu:** Data curation. **Guangri Jia:** Data curation. **Xuedong Fang:** Funding acquisition, Supervision, Writing - review & editing. **Fangfang Chen:** Funding acquisition, Supervision, Writing - review & editing. **Xiaoqiang Cui:** Funding acquisition, Supervision, Writing - review & editing.

Declaration of competing interest

The authors declare that they have no known competing financial interests or personal relationships that could have appeared to influence the work reported in this paper.

Acknowledgments

We greatly acknowledge the National Postdoctoral Program for Innovative Talents (BX20180117), the National Key Research and Development Program of China (2016YFA0200400), the National Natural Science Foundation of China (51571100, 51872116, 51702116,

51602305 and 31771093), the Program for JLU Science and Technology Innovative Research Team (JLUSTIRT, 2017TD-09, 2017TD-27, 2019TD-36), and the Project of International Collaboration of Jilin Province (201180414085GH).

Appendix A. Supplementary data

Supplementary data to this article can be found online at https://doi.org/10.1016/j.bios.2019.111697.

References

Alhabeb, M., Maleski, K., Anasori, B., Lelyukh, P., Clark, L., Sin, S., Gogotsi, Y., 2017. Chem. Mater. 29, 7633–7644.
Bai, X.R., Wang, L.H., Ren, J.Q., Bai, X.W., Zeng, L.W., Shen, A.G., Hu, J.M., 2019. Anal. Chem. 91, 2955–2963.
Cai, S.F., Xiao, W., Duan, H.H., Liang, X.X., Wang, C., Yang, R., Li, Y.D., 2018. Nano Res 11 (12), 6304–6315.
Chand, R., Ramalingam, S., Neethirajan, S., 2018. Nanoscale 10, 8217–8225.
Chen, Y.T., Ren, R., Pu, H.H., Chang, J.B., Mao, S., Chen, J.H., 2017. Biosens. Bioelectron. 89, 505–510.
Djire, A., Zhang, H.Y., Liu, J., Miller, E.M., Neale, N.R., 2019. ACS Appl. Mater. Interfaces 11, 11812–11823.
Frens, G., 1973. Nat. Phys. Sci. (Lond.) 241, 20–22.
Guo, C.P., Su, F.F., Song, Y.P., Hu, B., Wang, M.H., He, L.H., Peng, D.L., Zhang, Z.H., 2017. ACS Appl. Mater. Interfaces 9, 41188–41199.
Han, Q.Z., Wang, R.Y., Xing, B., Zhang, T., Khan, M.S., Wu, D., Wei, Q., 2018. Biosens. Bioelectron. 99, 493–499.
He, P., Wang, X.X., Cai, Y.Z., Shu, J.C., Zhao, Q.L., Yuan, J., Cao, M.S., 2019. Nanoscale 11, 6080.
Hedman, J., Klasson, M., Nilsson, R., Nordling, C., Sorokina, M.F., Kljushnikov, O.I., Nemnonov, S.A., Trapeznikov, V.A., Zyranov, V.G., 1971. Phys. Scr. 4, 195–201.
Hu, Y., Huang, Y.J., Wang, Z.G., Wang, Y.Y., Ye, X.X., Wong, W., Li, C.Y., Sun, D., 2018. Microchim. Acta 185, 570.
Jia, Y.J., Zhang, B., Chang, H.H., Yu, F.Y., Zhao, Z.H., 2019. J. Pharmaceut. Biomed. 169, 75–81.
Jie, G.F., Ge, J.J., Gao, X.S., Li, C.L., 2018. Biosens. Bioelectron. 118, 115–121.
Jun, B.M., Kim, S., Heo, J.Y., Park, C.M., Her, N., Jang, M., Huang, Y., Han, J.H., Yoon, Y., 2019. Nano Res 12 (3), 471–487.
Khalil, I., Yehye, W.A., Julkapli, N.M., Rahmati, S., Sina, A.A.I., Basirun, W.J., Johan, M.R., 2019. Biosens. Bioelectron. 131, 214–223.
Kumar, S., Umar, M., Saifi, A., Kumar, S., Augustine, S., Srivastava, S., Malhotra, B.D., 2019. Anal. Chim. Acta 1056, 135–145.
Lin, H., Wang, X.G., Yu, L.D., Chen, Y., Shi, J.L., 2017. Nano Lett. 17, 384–391.
Li, X., Li, Y.Q., Qiu, Q., Wen, Q.R., Zhang, Q., Yang, W.J., Yuwen, L.H., Weng, L.X., Wang, L.H., 2019. J. Colloid Interface Sci. 543, 96–105.
Lin, Y.Q., Li, L.B., Hu, L.L., Liu, K.Y., Xu, Y.N., 2014. Sens. Actuators B Chem. 202, 527–535.
Liu, H., Duan, C.Y., Yang, C.H., Shen, W.Q., Wang, F., Zhu, Z.F., 2015. Sens. Actuators B Chem. 218, 60–66.
Lv, H., Li, Y.Y., Zhang, X.B., Gao, Z.Q., Zhang, C.Y., Zhang, S., Dong, Y.H., 2018a. Biosens. Bioelectron. 112, 1–7.
Lv, H., Li, Y.Y., Zhang, X.B., Gao, Z.Q., Feng, J.H., Wang, P., Dong, Y.H., 2018b. Anal. Chim. Acta 1007, 61–70.
Lorencova, L., Bertok, T., Filip, J., Jerigova, M., Velic, D., Kasak, P., Mahmoud, K.A., Tkac, J., 2018. Sens. Actuators B Chem. 263, 360–368.
Majd, S.M., Salimi, A., Ghasemi, F., 2018. Biosens. Bioelectron. 105, 6–13.
Morales-Narváez, E., Merkoçi, A., 2019. Adv. Mater. 31, 1805043.
Muckley, E.S., Naguib, M., Ivanov, I.N., 2018. Nanoscale 10, 21689–21695.
Naguib, M., Kurtoglu, M., Presser, V., Lu, J., Niu, J., Heon, M., Hultman, L., Gogotsi, Y., Barsoum, M.W., 2011. Adv. Mater. 23 (37), 4248–4253.
Nie, G.M., Tang, Y., Zhang, B., Wang, Y., Guo, Q.F., 2018. Biosens. Bioelectron. 116, 60–66.
Oyedotun, K.O., Momodu, D.Y., Naguib, M., Mirghni, A.A., Masikhwa, T.M., Khaleed, A.A., Kebede, M., Manyala, N., 2019. Electrochim. Acta 301, 487–499.
Paniagua, G., Villalonga, A., Eguílaz, M., Vegas, B., Parrado, C., Rivas, G., Díez, P., Villalonga, R., 2019. Anal. Chim. Acta 1061, 84–91.
Parate, K., Karunakaran, C., Claussen, J.C., 2019. Sens. Actuators B Chem. 287, 165–172.
Peng, J.H., Chen, X.Z., Ong, W.J., Zhao, X.J., Li, N., 2019. Chem 5, 18–50.
Ren, X., Ma, H.M., Zhang, T., Zhang, Y., Yan, T., Du, B., Wei, Q., 2017. ACS Appl. Mater. Interfaces 9, 37637–37644.
Tang, D.P., Yuan, R., Chai, Y.Q., 2006. Bioproc. Biosyst. Eng. 28, 315–321.
Taniselass, S., Arshad, M.K.M., Gopinath, S.C.B., 2019. Biosens. Bioelectron. 130, 276–292.
Tian, Y., An, Y.L., Feng, J.K., 2019. ACS Appl. Mater. Interfaces 11, 10004–10011.
Tie, L.N., Yang, S.Y., Yu, C.F., Chen, H., Liu, Y.M., Dong, S.Y., Sun, J.Y., Sun, J.H., 2019. J. Colloid Interface Sci. 545, 63–70.
Tran, D.T., Hoa, V.H., Tuan, L.H., Kim, N.H., Lee, J.H., 2018. Biosens. Bioelectron. 119, 134–140.
Turner, N.H., Single, A.M., 1990. Surf. Interface Anal. 15, 215–222.
VahidMohammadi, A., Mojtabavi, M., Caffrey, N.M., Wanunu, M., Beidaghi, M., 2019. Adv. Mater. 31, 1806931.
Vashist, S.K., Dixit, C.K., MacCraithad, B.D., Kennedy, R.O., 2011. Analyst 136, 4431–4436.
Wang, H., Wang, X.M., Wang, J., Fu, W.L., Yao, C.Y., 2016. Sci. Rep. 6, 33140.
Wang, Y.J., Wei, Z.K., Luo, X.D., Wan, Q., Qiu, R.L., Wang, S.Z., 2019. Talanta 195, 33–39.
Wei, T., Zhang, X.Y., Zhang, Q., Yang, J.Q., Chen, Q., Wang, J.X., Li, X., Chen, J.Y., Ma, T., Li, G.G., Gao, S.L., Lou, J.Y., Que, R.S., Wang, Y., Dang, X.W., Zheng, L., Liang, T.B., Bai, X.L., 2019. Cancer Lett. 452, 237–243.
Wu, J.J., Lu, Y.L., Wu, Z.Q., Li, S., Zhang, Q., Chen, Z.T., Jiang, J., Lin, S.S., Zhu, L., Li, C.D., Liu, Q.J., 2018a. Sens. Actuators B Chem. 261, 279–287.
Wu, L.X., Lu, X.B., Dhanjai Wu, Z.S., Dong, Y.F., Wang, X.H., Zheng, S.H., Chen, J.P., 2018b. Biosens. Bioelectron. 107, 69–75.
Wu, Q., Song, D.Q., Zhang, D., Zhang, H., Ding, Y.Y., Yu, Y., Sun, Y., 2015. Microchim. Acta 182, 1739–1746.
Xiao, Z.B., Li, Z.L., Li, P.Y., Meng, X.P., Wang, R.H., 2019. ACS Nano 13, 3608–3617.
Xuan, J.N., Wang, Z.Q., Chen, Y.Y., Liang, D.J., Cheng, L., Yang, X.J., Liu, Z., Ma, R.Z., Sasaki, T., Geng, F.X., 2016. Angew. Chem. Int. Ed. 55, 14569–14574.
Xu, S.X., Liu, W., Hu, B.M., Wang, X.H., 2019. Nano Energy 58, 803–810.
Yuan, Y.L., Zhang, L., Wang, H.J., Chai, Y.Q., Yuan, R., 2018a. Anal. Chim. Acta 1001, 112–118.
Yuan, Y.F., Yu, X.T., Ouyang, Q.L., Shao, Y.H., Song, J., Qu, J.L., Yong, K.T., 2018b. 2D Mater. 5, 025015.
Zhang, H.X., Wang, Z.H., Zhang, Q.X., Wang, F., Liu, Y., 2019. Biosens. Bioelectron. 124-125, 184–190.
Zhang, Q.X., Wang, F., Zhang, H.X., Zhang, Y.Y., Liu, M.L., Liu, Y., 2018. Anal. Chem. 90, 12737–12744.
Zhou, L.Y., Zhang, X.N., Ma, L., Gao, J., Jiang, Y.J., 2017. Biochem. Eng. J. 128, 243–249.
Zeng, S., Baillargeat, D., Hod, H.P., Yong, K.T., 2014. Chem. Soc. Rev. 43, 3426–3452.